



# Reconstructing two-decadal global daily high-resolution XCO<sub>2</sub> records using a hybrid Transformer–BiLSTM model

5 Yu Qu<sup>1,2</sup>, Xian Shi<sup>3</sup>, Yulong Fan<sup>1,3</sup>, Zhihui Wang<sup>4,5</sup>, Jing Wei<sup>1\*</sup>

1. MEEKL-AERM, College of Environmental Sciences and Engineering, Institute of Tibetan Plateau, and Center for Environment and Health, Peking University, Beijing 100871, China.
2. School of Geographical Sciences, South China Normal University, Guangzhou, 510631, China.
- 10 3. College of Geodesy and Geomatics, Shandong University of Science and Technology, Qingdao 266590, China
4. University of Science and Technology of China, Hefei 230026, China
5. Anhui Province Key Laboratory of Optical Quantitative Remote Sensing, Hefei Institutes of Physical Science, Chinese Academy of Sciences, Hefei 230031, China

15

Correspondence: Jing Wei (jingwei@pku.edu.cn)

**Abstract:** Accurate and temporally continuous global observations of atmospheric carbon dioxide (XCO<sub>2</sub>) are essential for climate monitoring and emission assessment. However, satellite-based XCO<sub>2</sub> observations are often spatially incomplete and temporally discontinuous, while existing products typically suffer from coarse spatial resolutions, hindering the detection of fine-scale emission changes. Here, we developed a novel spatiotemporal Transformer-BiLSTM deep-learning network, which integrates the local temporal feature extraction capability of bidirectional long short-term memory with the global spatial dependency modeling strength of Transformer via self-attention mechanisms.

20 observations are often spatially incomplete and temporally discontinuous, while existing products typically suffer from coarse spatial resolutions, hindering the detection of fine-scale emission changes. Here, we developed a novel spatiotemporal Transformer-BiLSTM deep-learning network, which integrates the local temporal feature extraction capability of bidirectional long short-term memory with the global spatial dependency modeling strength of Transformer via self-attention mechanisms.

25 The network assimilates multisource data, from satellite observations, meteorological reanalysis, and precursor gases, to reconstruct global, daily, and seamless XCO<sub>2</sub> at 0.1° resolution from 2003 to 2022. Validation against independent Total Carbon Column Observing Network (TCCON) measurements shows excellent agreement, with a correlation coefficient ( $R^2$ ) value of 0.99, a root mean square error (RMSE) of 1.10 ppm, and a mean bias of 0.01 ppm. A subsequent bias correction scheme further

30 improves cross-satellite consistency, achieving a cross-validation coefficient of determination (CV-



$R^2$ ) of 0.99 and an RMSE of 0.97 ppm. Our dataset enables accurate characterization of daily  $XCO_2$  concentrations over global land surfaces, facilitating the detection of spatial heterogeneity associated with emission hotspots and point-source activities. The record reveals a persistent global increase in atmospheric  $XCO_2$  over the past two decades, with a mean growth rate of 2.24 ppm/yr ( $p < 0.001$ ). It reliably resolves global  $XCO_2$  variability across a wide range of temporal scales, from day-to-day fluctuations to long-term trends. It consistently captures large-scale climate-driven signals, such as ENSO-related interannual variability, and short-lived  $XCO_2$  enhancements associated with major wildfire events, demonstrating its capability to represent both persistent and episodic emission signals. This high-resolution, daily global  $XCO_2$  product (GlobalHigh $XCO_2$ ) provides a valuable benchmark for carbon cycle studies, atmospheric model evaluation, and emission monitoring, and is publicly available at <https://doi.org/10.5281/zenodo.18220961> (Qu and Wei, 2026).

## 1 Introduction

Carbon dioxide ( $CO_2$ ) is a principal greenhouse gas that plays a significant role in driving global climate change (Romanov, 2017). Driven by anthropogenic activities and extreme wildfires, the global mean atmospheric  $CO_2$  concentration reached  $419.31 \pm 0.15$  parts per million (ppm) in 2023, approximately 50% higher than preindustrial levels, making it a major contributor to ongoing climate change (Budget, 2023). In response to rising  $CO_2$  levels, the international community adopted the Paris Agreement in 2015, aiming to limit global warming to well below  $2^\circ C$  compared to preindustrial levels. Owing to its long atmospheric lifetime,  $CO_2$  accumulates in the atmosphere and exerts sustained radiative forcing, resulting in long-term climate impacts (Lee et al., 2023; Kemp et al., 2022). Accurate long-term monitoring of atmospheric  $CO_2$  is therefore essential for advancing understanding of the global carbon cycle, verifying national emission reduction commitments, and informing effective climate mitigation policies.

Atmospheric column-averaged dry air mole fractions of  $CO_2$  ( $XCO_2$ ) are commonly quantified using ground-based networks and satellite-based remote sensing techniques (Petzold et al., 2015; Huang et al., 2024a). Ground-based networks, such as the Total Carbon Column Observing Network (TCCON) provide accurate and stable point-based measurements; however, their sparse spatial distribution limits their ability to support refined assessments of the global carbon budget and regional carbon



fluxes (Li et al., 2024a). Satellite remote sensing offers a complementary approach by providing broad spatial coverage for regional and global-scale XCO<sub>2</sub> monitoring, but has a lower temporal sampling frequency (Buchwitz et al., 2015). Since the early 2000s, a series of satellite missions has progressively advanced XCO<sub>2</sub> observations in accuracy, spatial resolution, and temporal coverage.

65 The SCanning Imaging Absorption spectroMeter for Atmospheric CHartographY (SCIAMACHY) aboard the Environmental Satellite, launched in 2002, was the first satellite instrument to provide global XCO<sub>2</sub> observations till 2012 (Bovensmann et al., 1999). Subsequently, a new generation of spaceborne sensors, including Japan's Greenhouse Gas Observing Satellite (GOSAT) (Kuze et al., 2009; Butz et al., 2011) NASA's Orbiting Carbon Observatory-2/3 (OCO-2/3) (Crisp et al., 2017),

70 and China's TanSat (Yang et al., 2018), have substantially advanced top-down constraints on carbon sources and sinks. These satellite data have become indispensable for our understanding of large-scale carbon cycle processes. Despite major advances in satellite XCO<sub>2</sub> observations, existing products remain limited by cloud and aerosol contamination, surface effects, and orbital sampling constraints (He et al., 2022). These gaps severely restrict the accurate analysis of seasonal and

75 interannual changes in regional carbon fluxes and impede the detection of carbon-cycle anomalies associated with extreme climate events (Ma et al., 2021; Li et al., 2022).

To overcome spatial gaps in satellite XCO<sub>2</sub> observations, researchers have explored a variety of data fusion and reconstruction approaches. Early studies primarily relied on geospatial interpolation

80 techniques, such as kriging and its spatiotemporal extensions (Hammerling et al., 2012; He et al., 2020; Wang et al., 2025; Chen et al., 2024). While effective in data-rich regions, these methods often assume stationary spatial correlations, leading to large uncertainties in sparsely observed areas. Global reanalysis products, including CAMS and CarbonTracker, provide spatially complete fields but typically have coarse spatial resolution, limiting their ability to resolve regional emission sources

85 (Hua et al., 2024). Traditional machine learning (ML) models, such as Random Forest and XGBoost, have been widely adopted for XCO<sub>2</sub> reconstruction due to their strong nonlinear fitting capabilities (Ma et al., 2021; Zhang et al., 2023; Liang et al., 2023). However, these approaches generally treat reconstruction as point-wise regression problems, neglecting the intrinsic spatiotemporal autocorrelation and physical coherence of atmospheric fields, which often results in spatially and

90 temporally discontinuous outputs (Siabi et al., 2019; He et al., 2023b). Although some recent studies



have attempted to incorporate spatiotemporal information (Wang et al., 2020; Liu et al., 2024), their ability to capture long-range temporal dependencies and cross-regional teleconnections remains limited (He et al., 2023a). The rapid development of deep learning (DL) has created new opportunities for reconstructing atmospheric data, overcoming the limitations of conventional linear models (Wei  
95 et al., 2024). Spatiotemporally aware DL architectures, particularly those integrating convolutional neural networks (CNNs) with recurrent neural networks such as long short-term memory (LSTM), have demonstrated strong capabilities in capturing fine-scale spatial patterns and temporal dependencies (He et al., 2024; Zhang and Liu, 2023; Wu et al., 2024). Recent studies have leveraged these models to fuse multisource satellite data (Huang et al., 2024a), incorporate temporal sequence  
100 features for daily XCO<sub>2</sub> estimation (Tian et al., 2024), and generate high-resolution regional products using deep autoencoders (Antezana Lopez et al., 2025; Li et al., 2025).

Despite these methodological advances, generating a truly seamless global daily XCO<sub>2</sub> dataset remains challenging. Harmonizing long-term records from multiple satellite missions, including  
105 SCIAMACHY, GOSAT, and OCO-2, introduces inter-sensor inconsistencies due to differences in instrument design and retrieval algorithms (Li et al., 2022; Chen et al., 2024). Although TCCON observations have been used for post hoc harmonization in some studies (Huang et al., 2024b; Li et al., 2024b), bias correction is not yet fully integrated into the reconstruction framework. Moreover, existing global products often face a trade-off between spatial resolution and temporal frequency,  
110 providing either coarse daily fields or high-resolution monthly averages, thereby limiting their ability to capture short-term variability associated with extreme events such as wildfires (Liu et al., 2022; Rodrigues et al., 2025) and climate anomalies during El Niño episodes (Chatterjee et al., 2017; Betts et al., 2016). Consequently, a unified methodology that simultaneously addresses inter-satellite biases and captures long-range spatiotemporal dependencies at the global daily scale is still lacking.

115

To address these limitations, we develop a hybrid spatiotemporal deep learning framework based on a Transformer–BiLSTM architecture for global daily XCO<sub>2</sub> reconstruction. Through jointly learning temporal evolution and spatial coherence from multisource satellite observations, reanalysis data, and auxiliary predictors, the proposed approach effectively captures complex spatiotemporal variability  
120 in atmospheric XCO<sub>2</sub> fields. Leveraging this framework, we generate a seamless global daily XCO<sub>2</sub>



dataset at  $0.1^\circ$  resolution spanning 2003–2022. A TCCON-based bias correction strategy is incorporated to harmonize multiple satellite mission records and ensure long-term temporal consistency. In addition, explainable artificial intelligence techniques are employed to enhance model interpretability and to quantify the relative contributions of key drivers of XCO<sub>2</sub> variability. Together, these advances provide a consistent long-term XCO<sub>2</sub> product suitable for carbon-cycle analysis, emission monitoring, and climate-related applications.

## 2 Materials and methods

### 2.1 Multisource data

#### 2.1.1 Satellite, reanalysis, and ground-based XCO<sub>2</sub> data

Satellite-based XCO<sub>2</sub> retrievals from SCIAMACHY, GOSAT, and OCO-2 were used as the primary observational constraints in this study. SCIAMACHY, onboard ENVISAT and operating from 2002 to 2012, provided global XCO<sub>2</sub> observations at a resolution of  $30 \times 60$  km<sup>2</sup> approximately every 30 days, retrieved using the Bremen Optimal Estimation DOAS algorithm (BOED) (Bovensmann et al., 1999; Buchwitz et al., 2005; Reuter et al., 2011). GOSAT, launched in 2009, provides near-global coverage at 10.5 km<sup>2</sup> every three days through its Fourier Transform Spectrometer. OCO-2, operating since 2014, provides XCO<sub>2</sub> measurements at  $1.29 \times 2.25$  km<sup>2</sup> resolution every ~16 days using three grating spectrometers (Crisp, 2015). Here, we used the SCIAMACHY BOED products from 2003 to 2009, GOSAT Level 2 XCO<sub>2</sub> Version 9r products from 2010 to 2014, OCO-2 Level 2 XCO<sub>2</sub> Lite Version 11r product from 2015 to 2022. All retrievals underwent standard quality control, and only high-quality observations were retained. In addition, the Copernicus Atmosphere Monitoring Service (CAMS) provides a global atmospheric composition reanalysis, offering continuous greenhouse gas fields from 2003 to the present at  $0.75^\circ \times 0.75^\circ$  horizontal and three-hour temporal resolution (Agustí-Panareda et al., 2023). CAMS provides spatially complete and consistent estimates of large-scale XCO<sub>2</sub> patterns and was also employed in this study.

Ground-based observations were obtained from the TCCON, which provides high-precision column carbon dioxide (XCO<sub>2</sub>) measurements (average uncertainty ~0.2%), with sub-daily temporal sampling, typically consisting of multiple observations per clear-sky day, and are widely used to evaluate satellite retrievals (Wunch et al., 2017). We used all available 31 stations in the GGG2020





Shuttle Radar Topography Mission (SRTM) digital elevation model (DEM) at a spatial resolution of  
 175 90 m. [Table 1](#) provides an overview of all data sources used in this study.

Table 1. Summary of the data used for the XCO<sub>2</sub> reconstruction in our study.

Type	Source	Product	Spatial resolution	Temporal resolution	Period
Satellite	SCIAMACHY	XCO <sub>2</sub>	30×60 km <sup>2</sup>	~30 days	2003-2009
	GOSAT	XCO <sub>2</sub>	10.5 km <sup>2</sup>	~3 days	2010-2014
	OCO-2	XCO <sub>2</sub>	1.29×2.25 km <sup>2</sup>	~16 days	2015-2022
Meteorological variables	ERA5	Surface pressure (SP)	0.1°	Hourly	2003-2022
		2-meter temperature (T2M)			
		10m u wind (U10)			
		10m v wind (V10)			
		Surface net solar radiation (SNSR)			
		Total evaporation (ET)			
		Relative humidity (RH)			
Precursor	CAMS	CAMS-XCO <sub>2</sub>	0.75°	3-hour	2003-2022
		Nitrogen dioxide (NO <sub>2</sub> )	0.75°	3-hour	2003-2022
		CO	0.75°	3-hour	2003-2022
	Qu et al	GlobalHighXCH <sub>4</sub>	0.1°	Daily	2003-2022
	Surface-related variables	MODIS	NDVI	0.05°	Monthly
LST					
SRTM		Elevation	90 m	-	-

## 2.2 Model development and construction

### 180 2.2.1 Transformer-BiLSTM framework

In this study, we proposed a hybrid spatiotemporal Transformer-BiLSTM deep-learning framework to capture both temporal and spatial dependencies. Temporal sequences of all input predictors are first processed by a Bidirectional Long Short-Term Memory (Bi-LSTM) network, which encodes forward and backward dependencies to generate comprehensive temporal feature representations for  
 185 each grid cell, integrating both past and future context (Zhang et al., 2020). This sequence-to-sequence formulation captures temporal dependencies arising from diurnal cycles, synoptic weather variations, and seasonal biospheric processes affecting XCO<sub>2</sub> concentrations.

These temporally encoded features were then fed into the Transformer (Vaswani et al., 2017), which



190 models long-range spatial dependencies at regional and global scales via multi-head self-attention  
and position-wise feed-forward layers, without relying on local receptive fields. Each location's  
feature vector is projected into a Query, a Key, and a Value, and attention scores quantify the influence  
of every other location on that point. The multi-head mechanism integrates complementary spatial  
relationships across multiple subspaces, enabling the model to explicitly learn planetary-scale  
195 influences, such as atmospheric teleconnections and large-scale weather systems, on regional XCO<sub>2</sub>  
concentrations. The resulting spatiotemporal features are subsequently passed through a new  
multilayer perceptron (MLP) block, followed by a fully connected linear layer that projects the fused  
features to scalar daily XCO<sub>2</sub> values for each grid cell. To effectively capture the complex  
spatiotemporal dynamics of atmospheric XCO<sub>2</sub>, we designed a weighted spatiotemporal loss function  
200 that accounts for intrinsic temporal continuity and spatial correlation, in contrast to standard Mean  
Squared Error (MSE) loss functions:

$$L_{XCO_2} = \frac{1}{N} \sum_{i=1}^N (|y_i - \hat{y}_i| + \chi_1 * (|\Delta y_i - \Delta \hat{y}_i|) + \chi_2 * L_{spatial}) \quad (1)$$

205 where the first term ensures point-wise accuracy, the second term (weighted by  $\chi_1$ ) penalizes errors  
in temporal derivatives, and the third term (weighted by  $\chi_2$ ) enforces spatial smoothness via a  
Laplacian constraint. Optimal weights were determined via grid search ( $\chi_1 = 0.5, \chi_2 = 0.01$ ),  
ensuring robust reconstruction of seasonal cycles without over-smoothing high-emission features.

210 During model construction, the dataset was randomly partitioned into training, validation, and testing  
sets at a ratio of 8:1:1. The Bi-LSTM module consists of 64 hidden layers with a dimension of 128  
and a dropout rate of 0.5 to mitigate overfitting. The Transformer module comprises 4 encoder layers,  
each with 64-dimensional hidden layers and 4 attention heads, with ReLU activation functions  
applied between layers to enhance learning and facilitate sparse feature extraction. The Transformer-  
215 BiLSTM model was trained using the Adam optimizer with an initial learning rate of 0.001 and a  
batch size of 256. To optimize convergence, a learning rate scheduler reduced the rate by a factor of  
0.1 every 10 epochs if the validation loss did not improve. Training continued for up to 200 epochs,  
with early stopping applied if the validation loss failed to decrease for 15 consecutive epochs (Yeom



et al., 2021).

220

### 2.2.2 Two-phase reconstruction workflow

To address the spatial discontinuity of raw satellite observations and the limited coverage of TCCON ground-based stations, we designed a sequential two-phase “fusion-then-correction” reconstruction workflow (Fig. 2), decoupling spatial pattern learning from magnitude calibration.

225

**Phase 1: Data Fusion.** The goal of this stage is to generate a spatially continuous global XCO<sub>2</sub> field from sparse and discontinuous satellite swaths. The Transformer-BiLSTM model first takes XCO<sub>2</sub> retrievals from SCIAMACHY, GOSAT, and OCO-2 as the target and ingests multisource inputs, including atmospheric fields, i.e., XCH<sub>4</sub> from our previous study (Qu et al., 2025), CAMS XCO<sub>2</sub> and NO<sub>2</sub> concentrations; ERA5 meteorology variables (i.e., SP, T2M, SNSR, ET, U10, V10, BLH, RH); and surface or terrestrial variables (i.e., NDVI, LST, DEM). In addition, spatiotemporal encoding vectors are incorporated: spatial coordinates are represented by three Euclidean spherical functions ( $P_S$ ), and temporal dynamics by three helix-shaped trigonometric vectors ( $P_T$ ), enabling the model to capture spatial heterogeneity and temporal variability (Wei et al., 2023; Qu et al., 2025). The output of this phase is a preliminary fused daily XCO<sub>2</sub> estimates at 0.1°×0.1° resolution, providing a spatially continuous field to support the subsequent bias correction stage.

235

$$Fusion_{XCO_2} \sim f_{TF-BiLSTM}(CAMS_{XCO_2}, CAMS_{NO_2}, Qu_{XCH_4}, Pre_{gas}, Meteo, NDVI, LST, DEM, P_S, P_T) \quad (2)$$

**Phase 2: Bias Correction.** Satellite XCO<sub>2</sub> retrievals often exhibit systematic biases due to differences in sensor characteristics, retrieval algorithms, and temporal sampling. In this phase, the fused XCO<sub>2</sub> field from Phase 1 is further calibrated (bias-corrected) using TCCON ground-based measurements as reference standards. The Transformer-BiLSTM model ingests the fused XCO<sub>2</sub> data together with the same auxiliary predictors used in the fusion stage, including precursor gases (XCO<sub>2</sub>, XCH<sub>4</sub>, and NO<sub>2</sub>), meteorological variables, surface/terrestrial features, and spatiotemporal encoding vectors. By learning the complex nonlinear relationships between satellite-dependent biases and environmental conditions, this framework achieves robust global generalization. The output is a bias-corrected, gap-free, daily global XCO<sub>2</sub> dataset at 0.1° resolution, consistent across all satellite platforms:

245



$$Bias_{XCO_2} \sim f_{TF-BiLSTM}(Fusion_{XCO_2}, CAMS_{NO_2}, Qu_{XCH_4}, Pre_{gas}, Meteo, NDVI, LST, DEM, P_s, P_T) \quad (3)$$

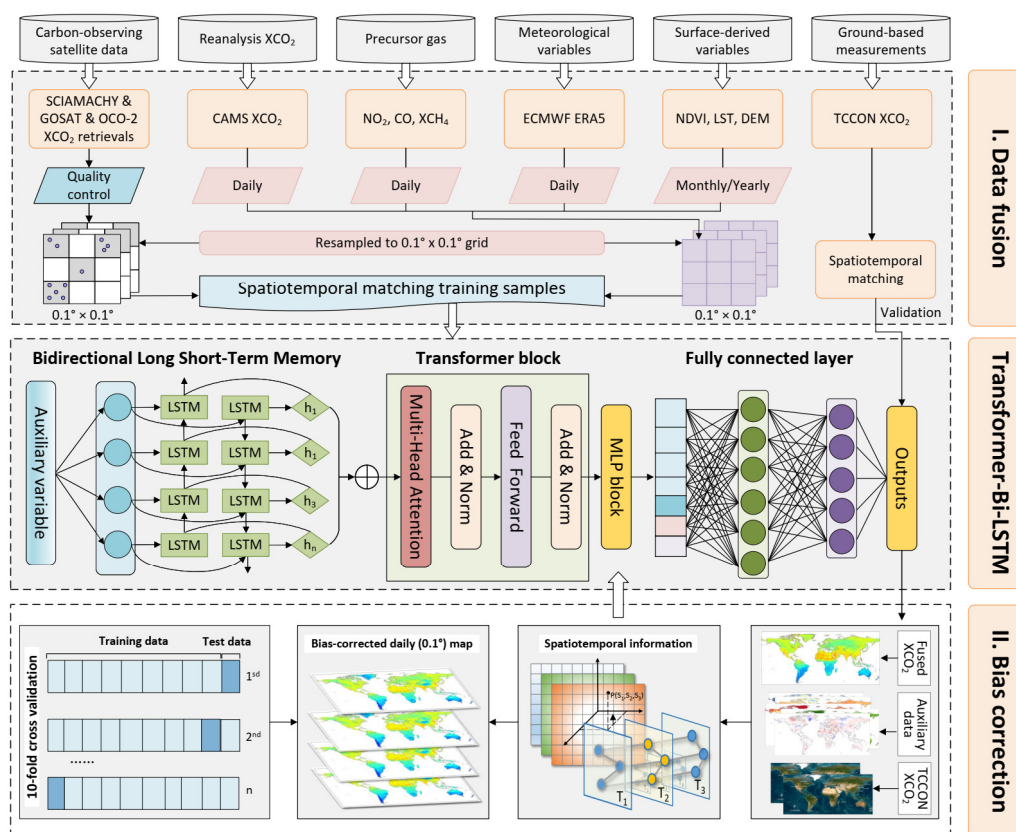


**Figure 2.** Workflow for generating global daily gapless XCO<sub>2</sub> concentrations with a 0.1°×0.1° resolution using the developed Transformer-BiLSTM framework.

255

### 2.3 Validation method

The data-fused XCO<sub>2</sub> estimates were independently evaluated against TCCON XCO<sub>2</sub> measurements. For both the data-fused and bias-corrected XCO<sub>2</sub> products, a multi-strategy ten-fold cross-validation (10-CV) framework was applied using satellite and TCCON observations. Specifically, the sample-based CV randomly withheld 10% of the daily grid-level samples to assess overall performance and internal consistency. Temporal-based CV withheld continuous blocks of daily data to evaluate the model's temporal generalization over periods without ground-based measurements. Spatial-based CV



withheld spatially contiguous clusters of grid cells ( $1^\circ \times 1^\circ$ ) to assess the model's capability to generalize in regions lacking ground-based observations.

265

### 3 Results and discussion

#### 3.1 Model performance

##### 3.1.1 Validation of data-fused XCO<sub>2</sub> estimates

We first evaluated the Transformer-BiLSTM model in the data-fusion phase using three 10-fold cross-validation approaches, comparing daily XCO<sub>2</sub> estimates with satellite retrievals from SCIAMACHY, GOSAT, and OCO-2 (Fig. 3). Sample-based CV show that our model accurately reconstructs daily XCO<sub>2</sub> concentrations across different satellite missions, as evidenced by increasing cross-validation R<sup>2</sup> (CV-R<sup>2</sup>) values from 0.91 (SCIAMACHY) to 0.96 (GOSAT) and 0.98 (OCO-2), and decreasing RMSE (MAE) values from 1.39 (1.03) to 0.82 (0.58) and 0.76 (0.53) ppm, reflecting improvements due to higher observation density and retrieval quality in later missions. Temporal-based CV further demonstrates stable predictive performance under interannual extrapolation, with CV-R<sup>2</sup> rising from 0.72 (SCIAMACHY) to 0.88 (GOSAT) and 0.93 (OCO-2), and RMSE (MAE) decreasing from 2.47 (1.43) to 1.45 (1.09) and 1.42 (1.05) ppm, indicating robust generalization across years and satellite transitions. Spatial-based CV confirms strong spatial predictive ability in under-monitored regions, with CV-R<sup>2</sup> increasing from 0.86 (SCIAMACHY) to 0.89 (GOSAT) and 0.96 (OCO-2), accompanied by RMSE (MAE) reduction from 1.71 (1.28) to 1.30 (0.98) and 1.10 (0.79) ppm.

270

275

280

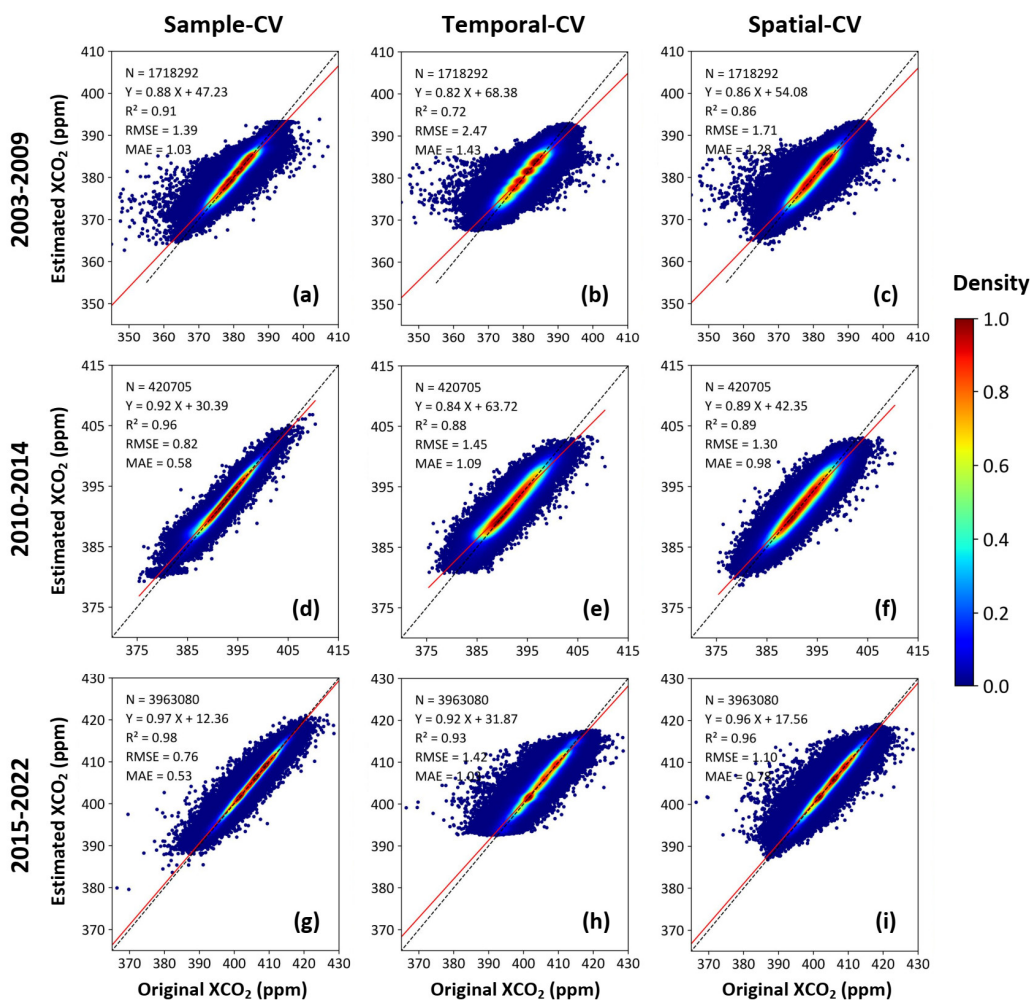
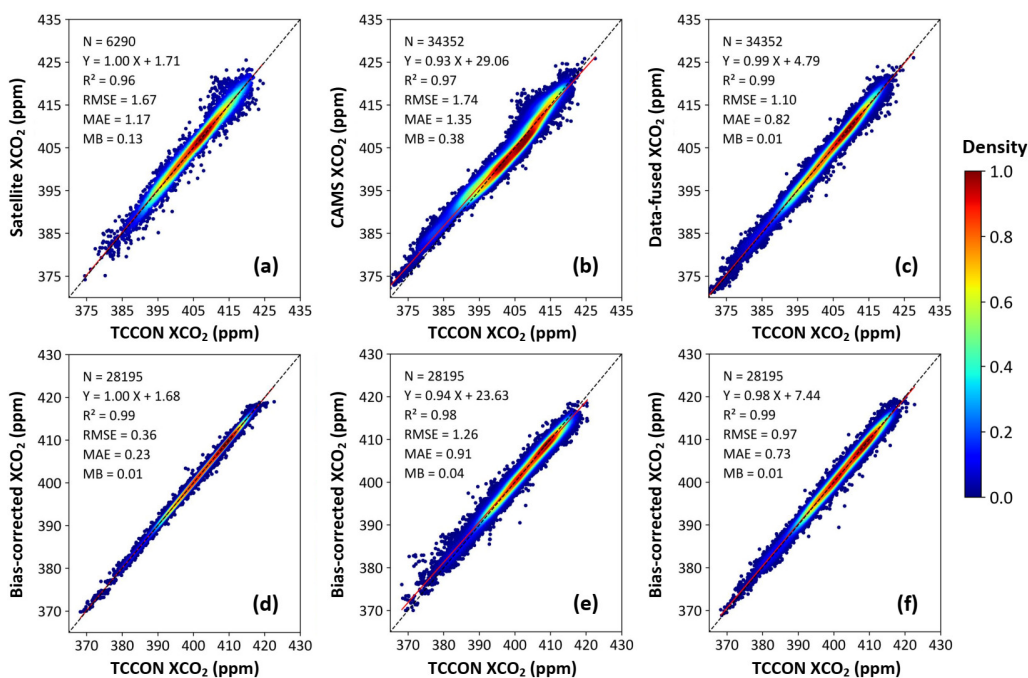


**Figure 3.** Density scatter plots of sample-based (left column), temporal-based (middle column), and spatial (right column) 10-fold cross-validation (CV) results for daily XCO<sub>2</sub> estimates during 2003-2009 (SCIAMACHY, top row), 2010-2014 (GOSAT, middle row), and 2015-2022 (OCO-2, bottom row). Dotted black dashed lines represent 1:1 lines, and solid red lines indicate linear regression fits.

Furthermore, we independently evaluated our data-fused XCO<sub>2</sub> estimates against TCCON ground-based measurements and compared their performance with satellite retrievals and CAMS reanalysis. Satellite XCO<sub>2</sub> observations show strong agreement with TCCON, yielding an R<sup>2</sup> of 0.96, an RMSE of 1.67 ppm, and a mean bias of 0.13 ppm (Fig. 4a). CAMS reanalysis exhibits a comparable correlation (R<sup>2</sup> = 0.97) but larger errors and a more pronounced systematic bias (RMSE = 1.74 ppm, mean bias = 0.38 ppm; Fig. 4b). In contrast, our data-fused XCO<sub>2</sub> achieves the best agreement with



295 TCCON, with an  $R^2$  of 0.99, an RMSE of 1.10 ppm, an MAE of 0.82 ppm, and a near-zero mean bias of 0.01 ppm (Fig. 4c), demonstrating that the fusion framework substantially improves consistency with ground-based observations.



300 **Figure 4.** Density scatterplots comparing daily XCO<sub>2</sub> concentrations from (a) satellite retrievals, (b) CAMS reanalysis, and (c) our data fusion approach against TCCON ground-based measurements, as well as 10-fold cross-validation (CV) results for our bias-corrected daily XCO<sub>2</sub> concentrations using (d) sample-based, (e) temporal-based, and (f) spatial-based ten-fold CV methods. Dotted black dashed lines represent 1:1 lines, and solid red lines indicate linear regression fits.

### 305 3.1.2 Validation of bias-corrected XCO<sub>2</sub> estimates

The bias-corrected XCO<sub>2</sub> estimates achieve excellent agreement with TCCON observations ( $R^2 = 0.99$ , RMSE = 1.03 ppm, MAE = 0.79 ppm) and a near-zero mean bias of 0.01 ppm, indicating that systematic biases in the data-fused data are effectively removed (Fig. 4d). Temporal-based CV further demonstrates stable predictive performance under interannual extrapolation: when continuous years are withheld from training, the bias-corrected XCO<sub>2</sub> achieves an  $R^2$  of 0.98, with an RMSE of 1.26 ppm, an MAE of 0.91 ppm, and a mean bias of 0.04 ppm (Fig. 4e), confirming stable temporal generalization across different years. Spatial-based CV confirms strong spatial transferability, with



an  $R^2$  of 0.99, an RMSE of 0.97 ppm, an MAE of 0.73 ppm, and a mean bias of 0.01 ppm (Fig. 4f), demonstrating reliable performance when extrapolating to under-monitored regions.

315

Beyond overall statistical accuracy, temporal seamlessness is critical when merging multi-decadal satellite records, particularly across mission transitions where systematic retrieval offsets can introduce artificial discontinuities. To evaluate the temporal stability of the reconstructed dataset across major satellite mission switch-overs (~2010 and ~2015), we conducted targeted diagnostics at long-term TCCON sites, including Garmisch (Europe) and Park Falls (North America) (Fig. 5). Daily XCO<sub>2</sub> time series spanning the SCIAMACHY–GOSAT and GOSAT–OCO-2 transitions reveal clear differences between the initial data-fused product and the bias-corrected reconstruction. At both sites, the uncorrected fused XCO<sub>2</sub> occasionally exhibits small but discernible step changes or systematic offsets coincident with mission switch-overs, indicating residual inter-mission inconsistencies. In contrast, the bias-corrected XCO<sub>2</sub> time series remains temporally smooth and continuous across the transition periods, with no apparent artificial discontinuities. Moreover, the corrected series closely follows TCCON observations in both seasonal phase and amplitude, preserving natural temporal variability while effectively eliminating sensor-induced biases. Together, these results highlight the robustness of the bias correction strategy in ensuring temporal seamlessness of the multi-decadal XCO<sub>2</sub> record.

320  
325  
330

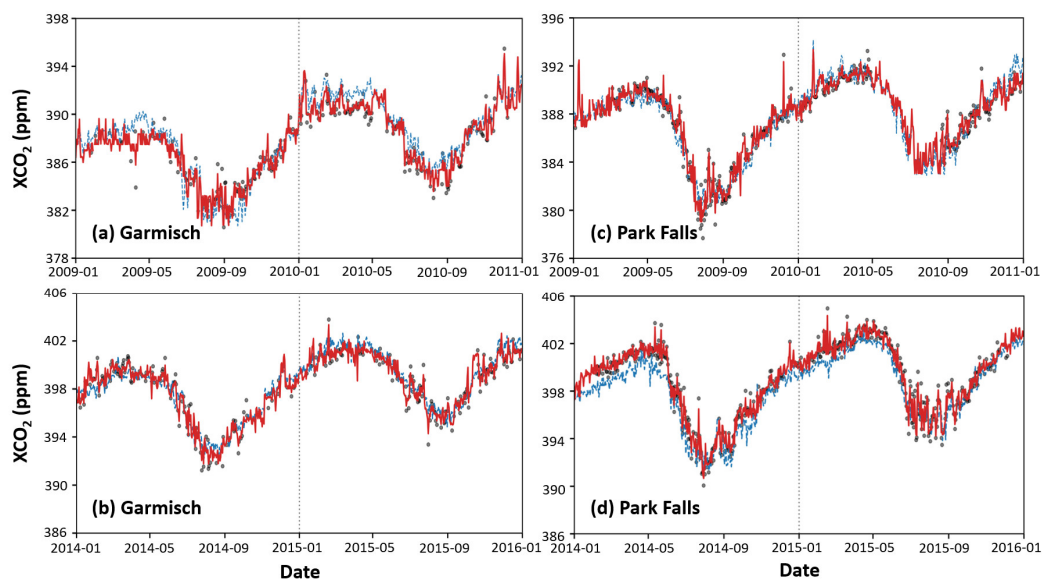
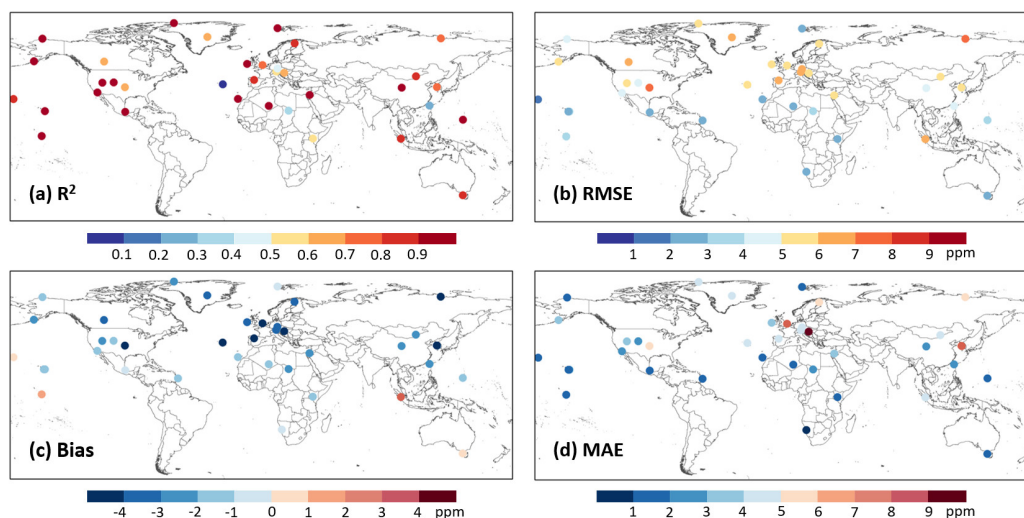


**Figure 5.** Time series of TCCON (grey dots), data-fused (blue dashed lines), and bias-corrected (red solid lines) XCO<sub>2</sub> data at the (a-b) Garmisch (Europe) and (c-d) Park Falls (North America) across key satellite transitions: (a) SCIAMACHY to GOSAT (2009-2010) and (b) GOSAT to OCO-2 (2014-2016). The vertical dotted lines mark the approximate times of satellite sensor transitions.

### 3.1.3 Independent validation with ObsPack network

To further evaluate the generalization ability of the bias-corrected daily XCO<sub>2</sub> dataset, we conducted an independent validation against surface flask measurements at 41 ObsPack stations from 2003 to 2022 (Fig. 6). The bias-corrected XCO<sub>2</sub> exhibits strong consistency with ObsPack observations, yielding a global mean R<sup>2</sup> of 0.86. More than 90% of the stations show high R<sup>2</sup> values exceeding 0.6, and over half (54%) exceed 0.9, indicating robust performance across diverse geographic and climatic conditions. Spatially, most stations (58%) show RMSE values ranging from 3 to 6 ppm, with larger values observed at stations in North America, Europe, and East Asia, where complex terrain and strong anthropogenic emissions dominate. Nonetheless, the estimated bias and MAE are generally low, with more than 73% and 80% of the stations within ± 3 ppm and below 5.0 ppm, respectively.



350 **Figure 6.** Global validation of our bias-corrected daily XCO<sub>2</sub> dataset against ObsPack surface flask observations during 2003-2022.

## 3.2 Spatiotemporal variations of global atmospheric XCO<sub>2</sub>

### 3.2.1 Global daily seamless XCO<sub>2</sub> maps

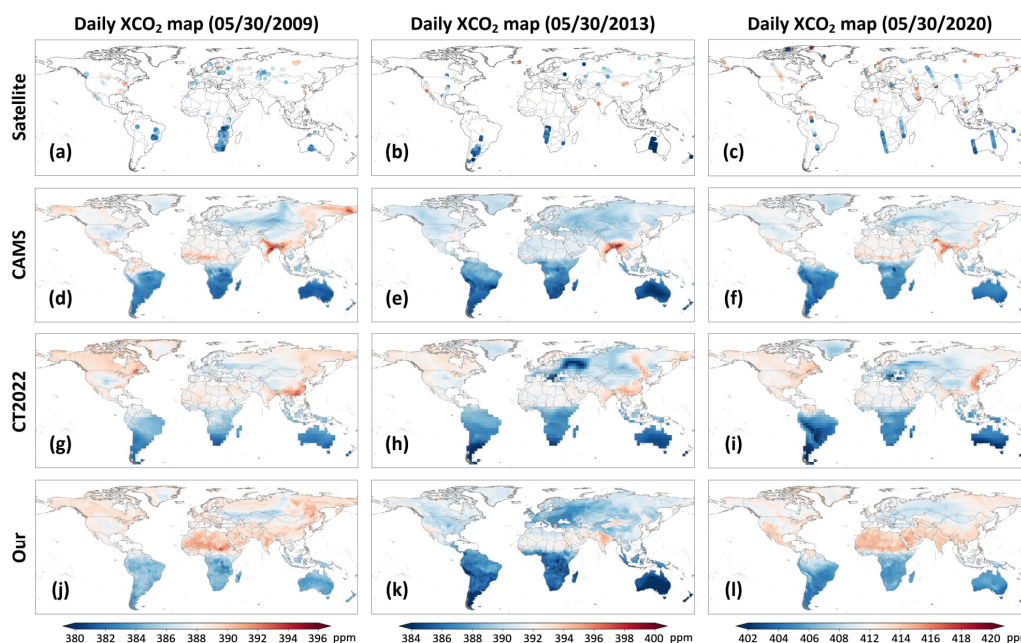
355 We compare global daily XCO<sub>2</sub> data derived from different products for three representative dates: May 30, 2009, 2013, and 2020 (Fig. 7). Satellite retrievals provide physically realistic XCO<sub>2</sub> signals but suffer from sparse and discontinuous spatial coverage due to orbital limitations and cloud contamination. CAMS (0.75°×0.75°) offers spatially complete fields but tends to weaken local spatial gradients, attenuating enhancements over major emission regions and underestimating background values in the Southern Hemisphere. CarbonTracker 2022 (CT2022, 3°×2°) is a widely used global CO<sub>2</sub> flux inversion system developed by NOAA to quantify atmospheric CO<sub>2</sub> sources and sinks using transport modeling (Jacobson et al., 2023). It captures large-scale interhemispheric gradients but exhibits regional inconsistencies, including exaggerated concentrations in parts of the Northern Hemisphere mid-latitudes and muted contrasts in tropical source regions. In contrast, our XCO<sub>2</sub> product achieves seamless global coverage while preserving fine-scale spatial heterogeneity and maintaining close consistency with satellite retrievals where available. Representative regional comparisons (highlighted by red circles) further illustrate these differences: In 2009, CT2022 overestimates XCO<sub>2</sub> over the eastern United States, while CAMS underestimates regional enhancements; our estimates closely match satellite observations. In 2013, both CAMS and CT2022

360

365



370 underestimate XCO<sub>2</sub> over northern China and southern Mongolia, whereas our product accurately  
captures the observed spatial patterns. In 2020, both CAMS and CT2022 underestimate XCO<sub>2</sub> over  
the Middle East, while our reconstruction reflects the enhanced concentrations in agreement with  
satellite observations. These examples demonstrate that our data provides a balanced and physically  
consistent representation of daily global XCO<sub>2</sub>, avoiding CAMS over-smoothing and the regional  
375 biases evident in CT2022.



380 **Figure 7.** Spatial distribution of global daily XCO<sub>2</sub> concentrations on May 30, 2009, 2013, 2020 from (a-c) SCIAMACHY, GOSAT, and OCO-2 satellites, (d-f) CAMS reanalysis, (g-i) CarbonTracker (CT2022), and (j-l) our reconstructed product.

### 3.2.2 Identification of localized CO<sub>2</sub> emission hotspots

Daily XCO<sub>2</sub> observations provide a distinct advantage for detecting localized and transient CO<sub>2</sub> emission hotspots that are often obscured in temporally averaged products (Fig. 8). Pronounced XCO<sub>2</sub> enhancements are detected over regions dominated by anthropogenic activities, including major industrial and energy-related sources such as steel production (Yokohama steel factory in Japan, f), coal mining (Arizona coal mine in USA, a), power generation (Electric power plant in Algerian, i), and chemical processing (Russia, d). Elevated XCO<sub>2</sub> concentrations are observed over industrial



clusters in East Asia, Central Asia (Muruntov oltin koni in Uzbekistan, **g**), Europe (Oil factory in  
390 Poland, **c**), North America, and the Middle East (Chemical industries in Saudi Arabia, **h**), consistent  
with known fossil-fuel combustion and extraction-related emissions. In addition to stationary sources,  
localized enhancements are also evident near major transport hubs, such as John F. Kennedy  
international airport in the US (**b**), reflecting the combined effects of urban activity and transportation  
emissions (Wang et al., 2020). Beyond anthropogenic sources, the daily XCO<sub>2</sub> dataset captures  
395 episodic natural emission events, such as forest fires (e.g., Xichang forest fire in China, **e**) and large-  
scale agricultural burning (Farmland fire in Brazil, **j**), which generate short-lived yet spatially  
coherent XCO<sub>2</sub> anomalies that are clearly resolved at daily timescales. These examples demonstrate  
that the reconstructed daily XCO<sub>2</sub> product effectively identifies both anthropogenic and natural CO<sub>2</sub>  
emission hotspots, resolves their spatial footprints, and supports the monitoring of localized emission  
400 dynamics at the global scale.

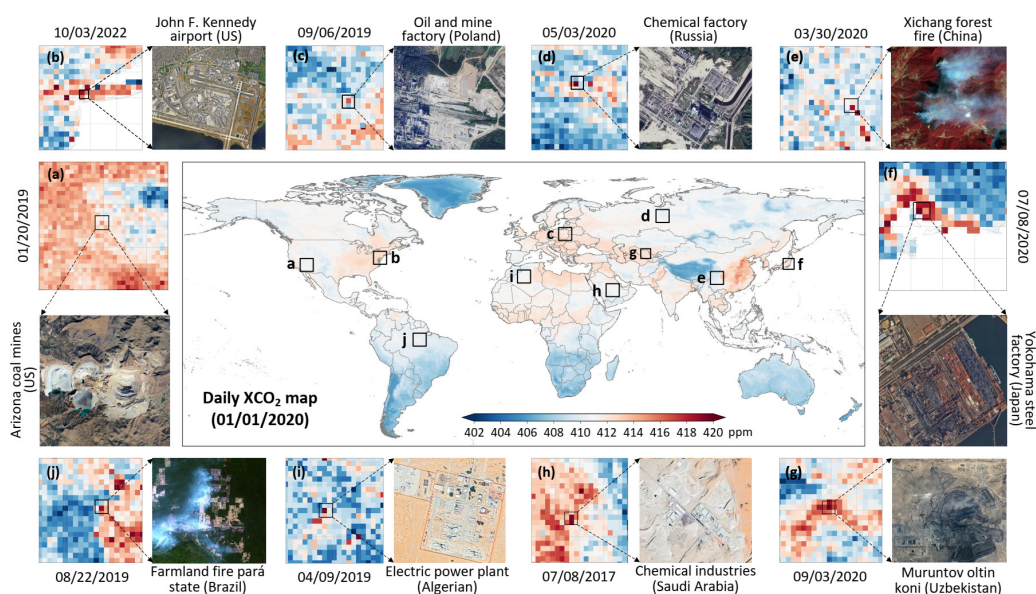


**Figure 8.** Detection of localized XCO<sub>2</sub> emission hotspots from our reconstructed global daily gapless  
dataset across (a-j) ten regions of interest on different days, with the central map showing the global  
405 distribution on January 1, 2020.

### 3.2.3 Impacts of biomass burning and ENSO on XCO<sub>2</sub> growth

Elevated fire-related CO<sub>2</sub> emissions and corresponding short-term XCO<sub>2</sub> anomalies are clearly



captured in our reconstructed dataset during extreme wildfire events. Over southeastern Australia (Fig. 9a), pronounced XCO<sub>2</sub> enhancements are observed from December 27, 2019, to January 8, 2020, coinciding with the peak of the 2019–2020 Australian bushfires. The daily XCO<sub>2</sub> time series exhibits a distinct local maximum on January 5, 2020 (average = 411.35 ± 0.56 ppm), superimposed on a gradually increasing background trend, with spatial distributions revealing significantly elevated concentrations over fire-affected regions. A similar short-term response is detected over Xichang City in southwestern China during the March–April 2020 wildfire episode (Fig. 9b), lasting over two weeks, from March 24 to April 8, 2020, with elevated daily XCO<sub>2</sub> concentrations. A clear local peak of 410.56 ± 0.53 ppm is observed on March 30, coinciding with the reported Xichang forest fire outbreak, followed by a gradual decline after April 5. These event-scale XCO<sub>2</sub> anomalies, resolved at daily resolution, demonstrate the dataset’s ability to capture rapid, short-lived carbon emissions and their impact on regional atmospheric XCO<sub>2</sub> variability.

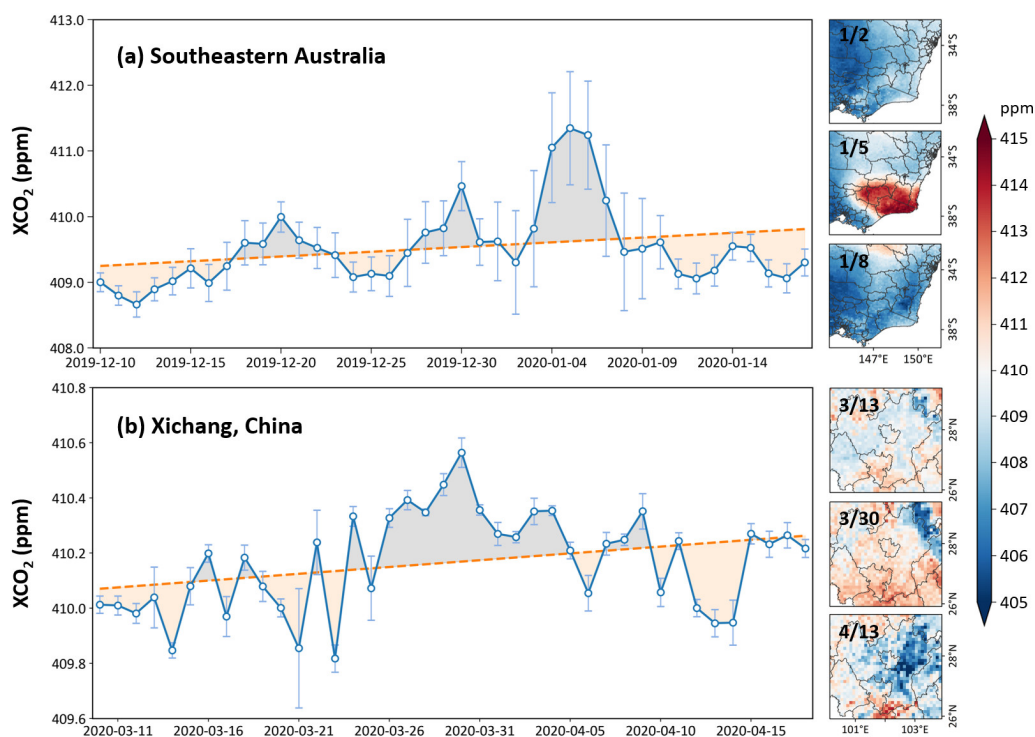
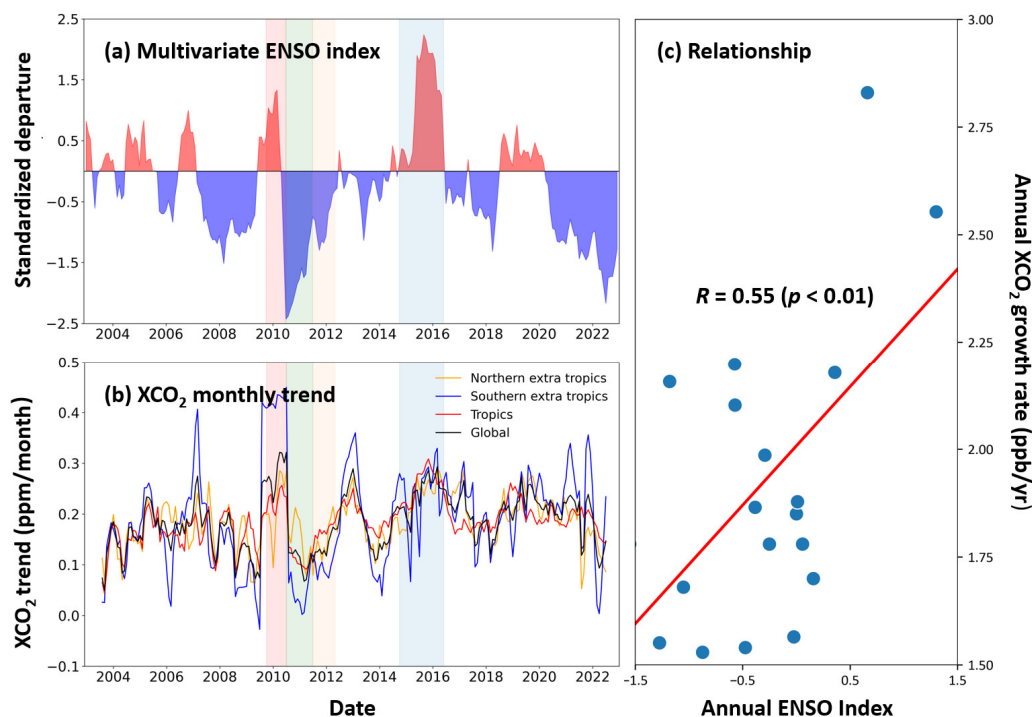


**Figure 9.** Time series and spatial distributions of daily XCO<sub>2</sub> concentrations associated with extreme wildfire events in (a) southeastern Australia (December 2019–January 2020) and (b) Xichang, China (March–April 2020).



Figure 10 shows that XCO<sub>2</sub> growth rates from our reconstructed dataset consistently respond to ENSO phases, as evidenced by the strong correlation with the multivariate ENSO index (MEI;  $R = 0.55$ ,  $p < 0.01$ ) (Wolter and Timlin, 2011), which explains ~34% of the observed interannual variability (Kim et al., 2016; Chatterjee et al., 2017). ENSO-driven anomalies in temperature and precipitation strongly regulate terrestrial carbon uptake and fire activity (Da Costa et al., 2024). During El Niño conditions, warmer and drier climates suppress ecosystem CO<sub>2</sub> absorption and enhance biomass burning, leading to elevated atmospheric growth rates (Betts et al., 2016; Guan et al., 2023; Ak-Bhd, 2021). This effect was most evident during the extreme 2015–2016 El Niño, which coincided with the highest recorded global XCO<sub>2</sub> growth rate of 3.11 ppm/yr ( $p < 0.001$ ) (Liu et al., 2024). In contrast, La Niña phases are generally cooler and wetter, strengthening terrestrial carbon sinks and reduce atmospheric growth rates, as observed in 2011–2012 and 2022 (Wang et al., 2014; Chatterjee et al., 2017). Regionally, ENSO sensitivity is highest in the tropics, where MEI explains ~45% of the interannual variability, highlighting the vulnerability of tropical forests to climate-induced stress and fire-related carbon losses (Brando et al., 2019; Liu et al., 2022). The Northern Extratropics show moderate sensitivity (~37%), while the Southern Extratropics are less affected (~27%), reflecting hemispheric differences in land–atmosphere coupling and fire regimes.



445 **Figure 10.** Time series of the monthly (a) multivariate ENSO index and (b) detrended XCO<sub>2</sub> trends over major regions: Northern extra tropics (30°N to 90°N), Southern extra tropics (90°S to 30°S), Tropics (30°S to 30°N), and Global. (c) Scatter plots between annual XCO<sub>2</sub> growth rates and the annual ENSO index. The La Niña of 2011 (LN11) is shaded in dark green. The preceding El Niño of 2010 (EN10) and succeeding weak La Niña of 2012 (LN12) are shaded in lighter red and green colors. The El Niño of 2015 (EN15) is shaded in dark blue.

450

### 3.2.4 Annual maps and long-term trends in global XCO<sub>2</sub>

Figure 11 shows the annual mean global XCO<sub>2</sub> from 2003 to 2022 over land, revealing a pronounced and sustained increase over the past two decades. During the early period (2003–2005), global XCO<sub>2</sub> levels are relatively low, with most regions characterized by concentrations below ~380 ppm. From 2006 to 2010, XCO<sub>2</sub> increases steadily across all continents, while spatial contrasts remain relatively modest. After approximately 2010, the spatial patterns intensify markedly. From 2011 to 2015, high-XCO<sub>2</sub> regions expand and strengthen, and from 2016 onward, the global increase accelerates further, with XCO<sub>2</sub> exceeding ~410 ppm over large portions of the Northern Hemisphere by 2018–2019 (Buchwitz et al., 2018; Lee et al., 2025). By 2022, nearly all continental regions display XCO<sub>2</sub> values above 415 ppm, with the highest concentrations concentrated over major industrialized and densely

460



populated regions in the Northern Hemisphere. Overall, the global mean XCO<sub>2</sub> increased monotonically from 374.54 ppm in 2003 to 416.36 ppm in 2022, corresponding to an increase of approximately 11% over the past 20 years. This substantial growth highlights the rapid accumulation of atmospheric CO<sub>2</sub> and the growing influence of anthropogenic emissions on the global carbon cycle.

465

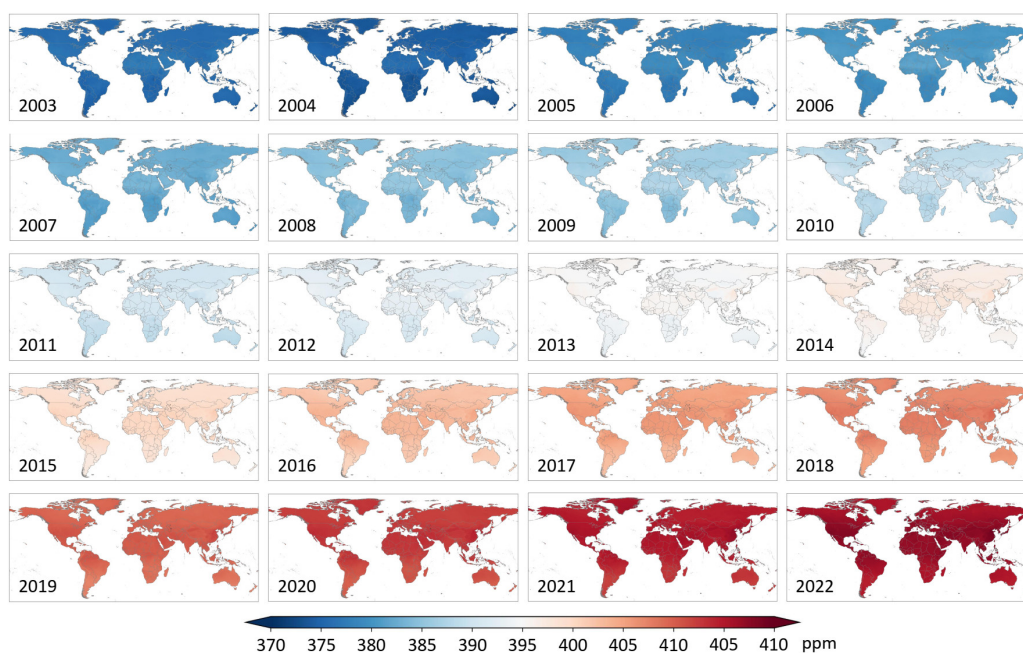


**Figure 11.** Spatial distribution of annual average XCO<sub>2</sub> concentrations (unit: ppm) over land from 2003 to 2022.

470 [Figure 12](#) presents the long-term (2003–2022) annual mean XCO<sub>2</sub> and seasonal climatology. The long-term global mean XCO<sub>2</sub> is  $394.58 \pm 0.76$  ppm, with a clear interhemispheric gradient characterized by higher concentrations in the Northern Hemisphere and lower values in the Southern. The highest XCO<sub>2</sub> concentrations are concentrated in the northern low- to mid-latitudes (~10–45°N), encompassing East and Southeast Asia, northern Africa and the Middle East, the United States, and parts of Europe and South Asia. These regions coincide with dense population centers, intensive industrial activity, and high fossil fuel consumption (Crippa et al., 2021; Sheng et al., 2021).  
475 Conversely, persistently low XCO<sub>2</sub> values occur over South America, central and southern Africa, and Australia, where strong biospheric uptake, sparse anthropogenic emissions, and the influence of



clean marine air masses suppress atmospheric CO<sub>2</sub> levels. At the national scale, South Korea exhibits  
480 the highest XCO<sub>2</sub> value ( $396.11 \pm 0.69$  ppm), followed by Kuwait ( $395.88 \pm 0.79$  ppm), consistent  
with intensive energy use and strong fossil fuel dependence.

Pronounced seasonal variability in XCO<sub>2</sub> is evident across global land (Fig. 12b-d). During boreal  
spring (MAM; average =  $395.36 \pm 2.20$  ppm), elevated XCO<sub>2</sub> concentrations are widespread across  
485 the Northern Hemisphere, reflecting accumulated winter emissions and the delayed onset of  
biospheric uptake. In boreal summer (JJA; average =  $392.74 \pm 1.29$  ppm), XCO<sub>2</sub> decreases markedly  
over northern high-latitude continents but increases in the Southern Hemisphere, forming extensive  
low-concentration bands associated with peak vegetation photosynthesis and strong net carbon uptake.  
Boreal autumn (SON; average =  $393.48 \pm 0.54$  ppm) is characterized by distinct enhancements over  
490 southern Africa, South America, and much of Australia, linked to biomass burning and reduced  
biospheric uptake. Seasonal amplitudes are particularly large in East Asia and the western United  
States (e.g., California), where intensive anthropogenic emissions coincide with strong biospheric  
seasonality (Sheng et al., 2021; Guan et al., 2024). In boreal winter (DJF, average =  $394.76 \pm 1.37$   
ppm), enhanced fossil fuel combustion and dormant vegetation lead to higher XCO<sub>2</sub> concentrations  
495 re-emerge across the Northern Hemisphere, whereas lower values prevail over Southern Hemisphere  
land and adjacent oceans, resulting in a pronounced hemispheric contrast.

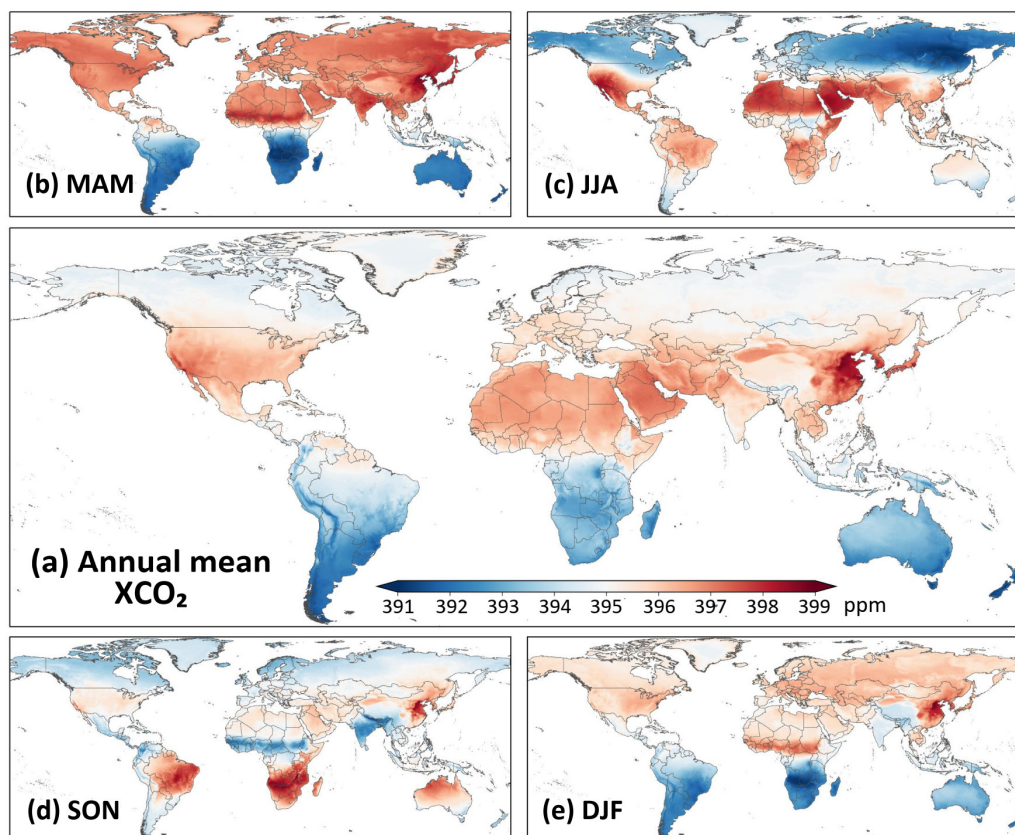
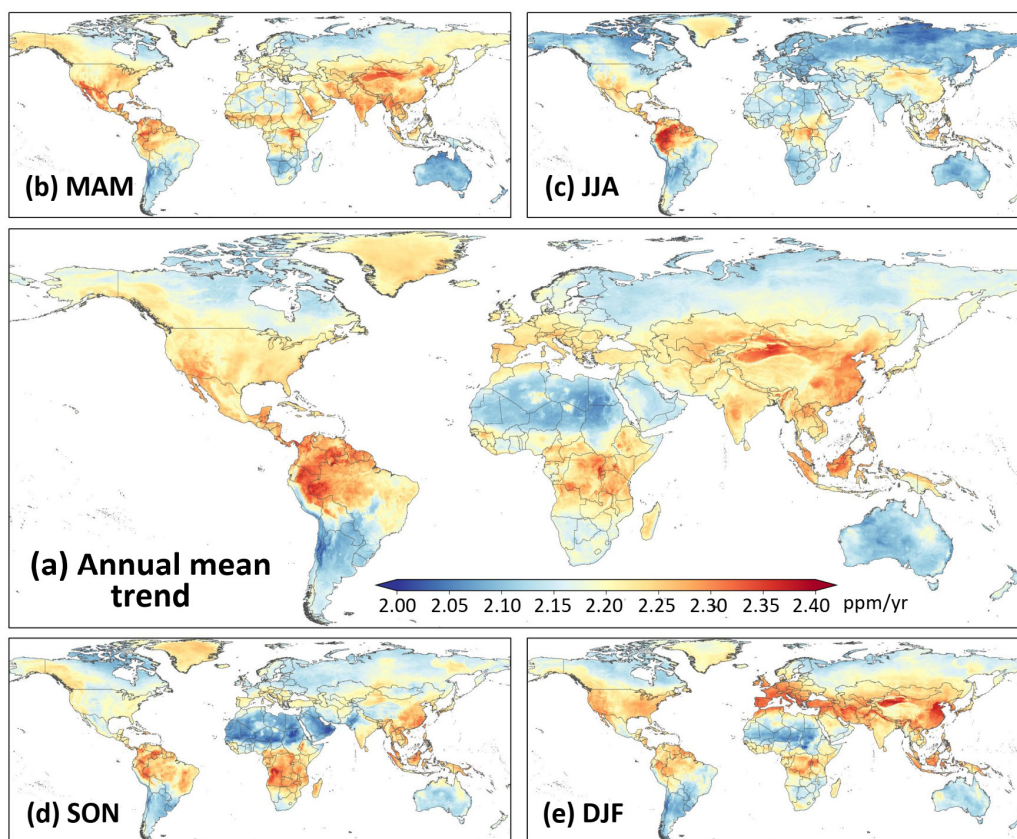


**Figure 12.** Multi-year (a) annual mean XCO<sub>2</sub> map (unit: ppm) over land for 2003–2022, and seasonal mean XCO<sub>2</sub> maps for (b) March–April–May (MAM), (c) June–July–August (JJA), (d) September–October–November (SON), and (e) December–January–February (DJF).  
500

**Figure 13** presents long-term XCO<sub>2</sub> trends from 2003 to 2022 across different temporal scales. All land regions exhibit significant increasing trends, with an average of 2.24 ppm/yr ( $p < 0.001$ ). The strongest increases ( $>2.25$  ppm/yr) occur over East and Southeast Asia, northern South America, and central Africa, while comparatively weaker growth ( $<2.15$  ppm/yr) is observed over southern South America, Australia, and the Sahara. Seasonal trends reveal distinct patterns (Fig. 13b–e). During MAM (average = 2.16 ppm/yr,  $p < 0.001$ ), large positive trends dominate the northern mid-latitudes, especially across much of Asia and North America, reflecting winter-emission accumulation and delayed biospheric uptake. In JJA (average = 2.23 ppm/yr,  $p < 0.001$ ), trends weaken over boreal and temperate regions but remain pronounced in the tropics, particularly the Amazon basin, central Africa, and Southeast Asia, corresponding to ongoing anthropogenic emissions and biomass burning. SON  
510



(average = 2.25 ppm/yr,  $p < 0.001$ ) shows enhanced trends over Africa and South America, forming clear regional maxima in biomass-burning regions, while northern mid-latitudes experience moderate growth. In DJF (average = 2.19 ppm/yr,  $p < 0.001$ ), trends intensify again across the Northern Hemisphere, notably in East Asia and Europe, driven by wintertime fossil fuel combustion, whereas the Southern Hemisphere shows weaker increases. Although the spring and winter seasons exhibit stronger regional contrasts, the autumn season shows a systematically higher spatially averaged XCO<sub>2</sub> growth trend, indicating a more widespread enhancement rather than localized extremes.



520

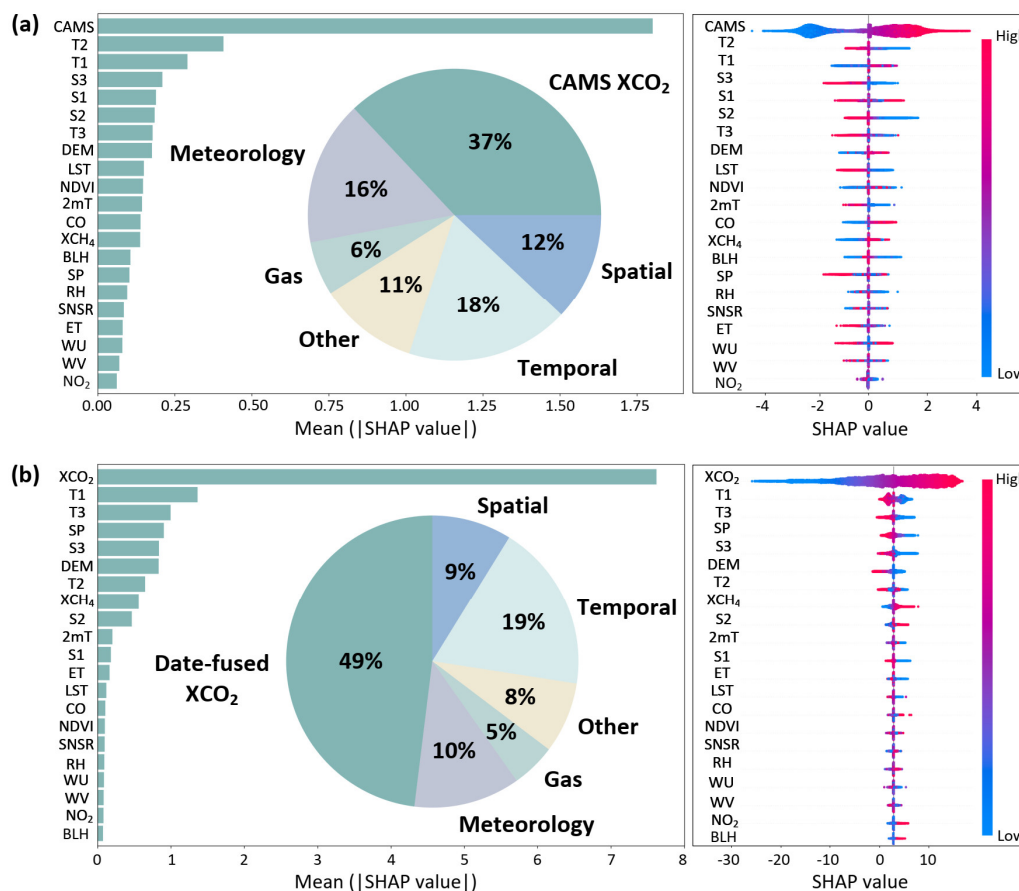
**Figure 13.** Spatial patterns of long-term annual XCO<sub>2</sub> trends (unit: ppm/yr) from 2003 to 2022, and seasonal XCO<sub>2</sub> trends (unit: ppm/yr) for (b) March–April–May (MAM), (c) June–July–August (JJA), (d) September–October–November (SON), and (e) December–January–February (DJF).



## 525 3.3 Discussion

### 3.3.1 Model interpretation with XAI

To improve model transparency and quantify the relative importance of input variables, we applied SHapley Additive exPlanations (SHAP) to the trained 4D-STransformer-BiLSTM model (Lundberg and Lee, 2017). The SHAP values were calculated to assess the contribution of each predictor to the reconstructed XCO<sub>2</sub> fields. For the data-fusion stage (Fig. 14a), the CAMS XCO<sub>2</sub> emerges as the dominant contributor, accounting for 37% of the total importance, reflecting its role in providing a temporally continuous and spatially coherent background field. Spatiotemporal encoding variables collectively contribute 30%, highlighting the importance of explicitly representing spatial structure and temporal dynamics in global XCO<sub>2</sub> reconstruction. Meteorological variables (16%) and satellite-derived surface variables (11%) provide complementary information that refines regional-scale variability, while precursor gases contribute a smaller but non-negligible share (6%). For the bias-correction stage (Fig. 14b), the fused XCO<sub>2</sub> field dominates the model output, contributing 49%, consistent with its role as the primary constraint for harmonizing inter-satellite differences using TCCON observations. Temporal indicators (19%), spatial variables (9%), and meteorological variables (10%) further capture systematic temporal, spatial, and environmental patterns in satellite retrieval biases. Overall, the XAI analysis indicates that the proposed framework is primarily constrained by physically meaningful background information, while auxiliary variables are effectively integrated to refine spatiotemporal XCO<sub>2</sub> structures and reduce systematic biases.



545 **Figure 14.** Model interpretability analysis using the SHAP approach, showing the relative importance  
 of each predictive factor for the (a) data-fused stage and (b) bias-corrected stage.

### 3.3.2 Comparison with previous studies

We compared our reconstructed XCO<sub>2</sub> dataset with previous global XCO<sub>2</sub> reconstruction studies that  
 550 applied out-of-sample validation against TCCON observations (Table 2). Some studies are limited to  
 coarser temporal resolutions at monthly (Zhang et al., 2023; Wang et al., 2025), 8-day (Li et al., 2022;  
 Guan et al., 2024), or 3-day (Sheng et al., 2023) scales, which limits their ability to capture short-  
 term (daily) variability. In addition, many studies generated XCO<sub>2</sub> at coarser spatial resolutions  
 (≥0.25°), limiting their representation of localized emission gradients and subregional heterogeneity  
 555 (Li et al., 2022; Sheng et al., 2023; Jin et al., 2022; Gao et al., 2023; Huang et al., 2024c; Wang et al.,  
 2023). Many products cover only limited periods (usually <10 years) after 2014, constraining  
 analyses of long-term historical trends (Sheng et al., 2023; Huang et al., 2024c). More importantly,



previous studies exhibit larger fluctuations in overall accuracy, with  $CV-R^2$  ranging from 0.83 to 0.98 and RMSEs from 0.95 to 2.62 ppm, reflecting methodological limitations. In contrast, our 4D-Transformer–BiLSTM framework reconstructs a global, seamless, daily  $XCO_2$  dataset at a  $0.1^\circ$  spatial resolution over 2003–2022, achieving  $R^2$  of 0.99 and RMSE of 1.10 ppm, which represents a clear advancement over existing  $XCO_2$  datasets.

**Table 2.** Comparison of reconstructed global  $XCO_2$  datasets from previous studies.

Method	Temporal	Spatial	$R^2$	RMSE	Time frame	Literature
DINEOF-BME	Monthly	$1^\circ$	0.92	1.60	2010-2020	Gao et al. (2023)
Deep forest	Monthly	$0.1^\circ$	0.96	0.95	2014-2020	Zhang et al. (2023)
At-Bi-LSTM	Monthly	$0.05^\circ$	0.92	1.54	2015-2021	Wang et al. (2025)
Extreme tree	8-day	$0.01^\circ$	0.83	1.79	2014-2018	Li et al. (2022)
Stacking model	8-day	$0.05^\circ$	0.98	1.03	2000-2020	Guan et al. (2024)
Kriging	3-day	$1^\circ$	0.97	0.88	2009-2023	Sheng et al. (2023)
M-FRK	Daily	$1^\circ$	0.93	1.06	2016-2019	Huang et al. (2024c)
Self-supervised	Daily	$0.25^\circ$	0.93	0.18	2010-2020	Wang et al. (2023)
DINCAE	Daily	$0.1^\circ$	0.90	1.44	2018-2022	Antezana Lopez et al. (2025)
MLE	3-h	$0.5^\circ$	0.92	2.62	2003-2020	Jin et al. (2022)
This study	Daily	$0.1^\circ$	0.99	1.10	2003-2022	-

DINEOF-BME: Data Interpolation Empirical Orthogonal Function- Bayesian Maximum Entropy; At-Bi-LSTM: Attention bidirectional long short-term memory; M-FRK: Multiscale fixed rank kriging; DINCAE: Data Interpolating Empirical Orthogonal Functions and Convolutional Auto-Encoder; MLE: Maximum likelihood estimation.

#### 4 Conclusions

Accurate, high-resolution observations of atmospheric  $XCO_2$  are critical for understanding the global carbon cycle, quantifying anthropogenic emissions, and supporting climate mitigation strategies. This study develops a novel Transformer–BiLSTM framework to reconstruct a global, daily, and spatially seamless  $XCO_2$  dataset at  $0.1^\circ$  resolution covering 2003–2022. By jointly integrating multi-mission satellite retrievals, CAMS reanalysis, meteorological variables, and precursor gas information, the framework effectively bridges spatial gaps and temporal discontinuities inherent in individual satellite records. A dedicated spatiotemporal loss formulation enforces continuity across space and time, and a bias-correction strategy is applied to harmonize inter-satellite differences and generate a physically consistent long-term  $XCO_2$  record.

580



Comprehensive validation demonstrates that the reconstructed dataset achieves high accuracy and robustness, as evidenced by independent evaluation against TCCON observations after data fusion ( $R^2 = 0.99$ , RMSE = 1.10 ppm), and ten-fold cross-validation after bias correction ( $CV-R^2 = 0.99$ , RMSE = 0.97 ppm). Using the daily XCO<sub>2</sub> data, we are able to capture rapid variations and identify  
585 localized XCO<sub>2</sub> emission hotspots from diverse sources, including urban activities, industrial emissions, and biomass burning. The dataset also effectively reflects strong responses of XCO<sub>2</sub> growth to major climate events, such as intense El Niño episodes and large-scale wildfire events. Across temporal scales, XCO<sub>2</sub> exhibits a long-term increasing trend of ~2.24 ppm/yr ( $p < 0.001$ ) from  
2003 to 2022, with the larger growth rates observed over northern South America, East and Southeast  
590 Asia, and central Africa, and weaker growth over southern South America, Australia, and the Sahara. This high-resolution, daily global dataset provides a robust tool for analyzing both long-term trends and short-term variability, offering valuable insights for carbon-cycle research, emission monitoring, and climate mitigation assessments. Future improvements may include enhancing XCO<sub>2</sub> retrievals using higher-resolution satellite observations, better representing natural and, in particular, urban  
595 emissions, and expanding ground-based validation networks.

### Data availability

The SCIAMACHY, GOSAT XCO<sub>2</sub>, and OCO-2/3 XCO<sub>2</sub> datasets are available at <https://data.ceda.ac.uk/neodc/esacci/ghg/data>, <https://disc.gsfc.nasa.gov/>, and  
600 <https://disc.gsfc.nasa.gov/>, respectively. The Copernicus Climate Data Store provides the CAMS-EGG4 XCO<sub>2</sub> product at <https://ads.atmosphere.copernicus.eu/datasets>, and ERA5 reanalysis data are available at <https://cds.climate.copernicus.eu/datasets>. The global daily high-resolution XCH<sub>4</sub> dataset (GlobalHighXCH<sub>4</sub>) is available at <https://doi.org/10.5281/zenodo.15492399>. MODIS products can be accessed at <https://ladsweb.modaps.eosdis.nasa.gov/search>. The global daily high-resolution  
605 XCO<sub>2</sub> product (GlobalHighXCO<sub>2</sub>) is publicly available at <https://doi.org/10.5281/zenodo.18220961> (Qu and Wei, 2026).

### Financial support

This work was partially supported by the National Key Technology and Development Program of  
610 Corps (2025AA001), and the Scientific Research Innovation Project of Graduate School of South



China Normal University (No.2025KYLX064).

### Acknowledgments

The authors acknowledge the data providers whose datasets were used in this study.

615

### Author contributions

YQ, XS, YF, ZW collected the data, conducted the formal analysis, performed the research, and wrote the initial draft of this paper. JW managed project administration, supervised the project, acquired funding.

620

### Competing interests

At least one of the (co-)authors is a member of the editorial board of *Earth System Science Data*.

### References:

- 625 Agustí-Panareda, A., Barré, J., Massart, S., Inness, A., Aben, I., Ades, M., Baier, B. C., Balsamo, G., Borsdorff, T., and Bousserez, N.: The CAMS greenhouse gas reanalysis from 2003 to 2020, *Atmospheric Chemistry and Physics*, 23, 3829-3859, 2023.
- Ak-Bhd, M.: WMO greenhouse gas bulletin, World Meteorological Organization: Geneva, Switzerland, 2021.
- 630 Antezana Lopez, F. P., Zhou, G., Jing, G., Zhang, K., Chen, L., Chen, L., and Tan, Y.: Global Daily Column Average CO<sub>2</sub> at 0.1°× 0.1° Spatial Resolution Integrating OCO-3, GOSAT, CAMS with EOF and Deep Learning, *Scientific Data*, 12, 268, 2025.
- Betts, R. A., Jones, C. D., Knight, J. R., Keeling, R. F., and Kennedy, J. J.: El Niño and a record CO<sub>2</sub> rise, *Nature Climate Change*, 6, 806-810, 2016.
- 635 Bovensmann, H., Burrows, J., Buchwitz, M., Frerick, J., Noel, S., Rozanov, V., Chance, K., and Goede, A.: SCIAMACHY: Mission objectives and measurement modes, *Journal of the atmospheric sciences*, 56, 127-150, 1999.
- Brando, P. M., Paolucci, L., Ummenhofer, C. C., Ordway, E. M., Hartmann, H., Cattau, M. E., Rattis, L., Medjibe, V., Coe, M. T., and Balch, J.: Droughts, wildfires, and forest carbon cycling: A pantropical synthesis, *Annual Review of Earth and Planetary Sciences*, 47, 555-581, 2019.
- 640 Buchwitz, M., De Beek, R., Noël, S., Burrows, J., Bovensmann, H., Bremer, H., Bergamaschi, P., Körner, S., and Heimann, M.: Carbon monoxide, methane and carbon dioxide columns retrieved from SCIAMACHY by WFM-DOAS: year 2003 initial data set, *Atmospheric Chemistry and Physics*, 5, 3313-3329, 2005.
- 645 Buchwitz, M., Reuter, M., Schneising, O., Boesch, H., Guerlet, S., Dils, B., Aben, I., Armante, R., Bergamaschi, P., and Blumenstock, T.: The Greenhouse Gas Climate Change Initiative (GHG-CCI): Comparison and quality assessment of near-surface-sensitive satellite-derived CO<sub>2</sub> and CH<sub>4</sub> global data sets, *Remote Sensing of Environment*, 162, 344-362, 2015.
- Buchwitz, M., Reuter, M., Schneising, O., Noël, S., Gier, B., Bovensmann, H., Burrows, J. P., Boesch, H., Anand, J., and Parker, R. J.: Computation and analysis of atmospheric carbon dioxide annual
- 650



- mean growth rates from satellite observations during 2003–2016, *Atmospheric Chemistry and Physics*, 18, 17355–17370, 2018.
- Budget, G. C.: Global carbon budget 2023, *Earth Syst. Sci. Data*, 15, 5301–5369, <https://doi.org/10.5194/essd-15-5301-2023>, 2023.
- 655 Butz, A., Guerlet, S., Hasekamp, O., Schepers, D., Galli, A., Aben, I., Frankenberg, C., Hartmann, J. M., Tran, H., and Kuze, A.: Toward accurate CO<sub>2</sub> and CH<sub>4</sub> observations from GOSAT, *Geophysical Research Letters*, 38, 2011.
- Chatterjee, A., Gierach, M., Sutton, A., Feely, R., Crisp, D., Eldering, A., Gunson, M., O’Dell, C., Stephens, B., and Schimel, D.: Influence of El Niño on atmospheric CO<sub>2</sub> over the tropical Pacific Ocean: Findings from NASA’s OCO-2 mission, *Science*, 358, eaam5776, 2017.
- 660 Chen, J., Hu, R., Chen, L., Liao, Z., Che, L., and Li, T.: Multi-sensor integrated mapping of global XCO<sub>2</sub> from 2015 to 2021 with a local random forest model, *ISPRS Journal of Photogrammetry and Remote Sensing*, 208, 107–120, 2024.
- Crippa, M., Guizzardi, D., Pisoni, E., Solazzo, E., Guion, A., Muntean, M., Florczyk, A., Schiavina, M., Melchiorri, M., and Hutfilter, A. F.: Global anthropogenic emissions in urban areas: patterns, trends, and challenges, *Environmental Research Letters*, 16, 074033, 2021.
- Crisp, D.: Measuring atmospheric carbon dioxide from space with the Orbiting Carbon Observatory-2 (OCO-2), *Earth Observing Systems XX*, 960702, 2015.
- Crisp, D., Pollock, H. R., Rosenberg, R., Chapsky, L., Lee, R. A., Oyafuso, F. A., Frankenberg, C., O’Dell, C. W., Bruegge, C. J., and Doran, G. B.: The on-orbit performance of the Orbiting Carbon Observatory-2 (OCO-2) instrument and its radiometrically calibrated products, *Atmospheric Measurement Techniques*, 10, 59–81, 2017.
- 670 da Costa, L. M., de Araújo Santos, G. A., de Mendonça, G. C., de Souza Maria, L., da Silva Jr, C. A., Panosso, A. R., and La Scala Jr, N.: Exploring CO<sub>2</sub> anomalies in Brazilian biomes combining OCO-2 & 3 data: Linkages to wildfires patterns, *Advances in Space Research*, 73, 4158–4174, 2024.
- Gao, Z., Jiang, Y., He, J., and Wu, J.: Spatiotemporal variation analysis of global XCO<sub>2</sub> concentration during 2010–2020 based on DINEOF-BME framework and wavelet function, *Science of The Total Environment*, 892, 164750, 2023.
- 680 Guan, X., Sun, Z., Chu, D., Xie, G., Wang, Y., and Shen, H.: Long-term (2000–2020) global 0.05° continuous atmospheric carbon dioxide mapping combining OCO-2 observations and model simulations, *Science of The Total Environment*, 957, 177051, 2024.
- Guan, Y., Keppel-Aleks, G., Doney, S. C., Petri, C., Pollard, D., Wunch, D., Hase, F., Ohyama, H., Morino, I., and Notholt, J.: Characteristics of interannual variability in space-based XCO<sub>2</sub> global observations, *Atmospheric Chemistry and Physics*, 23, 5355–5372, 2023.
- 685 Hammerling, D. M., Michalak, A. M., and Kawa, S. R.: Mapping of CO<sub>2</sub> at high spatiotemporal resolution using satellite observations: Global distributions from OCO-2, *Journal of Geophysical Research: Atmospheres*, 117, 2012.
- He, C., Ji, M., Li, T., Liu, X., Tang, D., Zhang, S., Luo, Y., Grieneisen, M. L., Zhou, Z., and Zhan, Y.: Deriving full-coverage and fine-scale XCO<sub>2</sub> across China based on OCO-2 satellite retrievals and CarbonTracker output, *Geophysical Research Letters*, 49, e2022GL098435, 2022.
- 690 He, Q., Ye, T., Chen, X., Dong, H., Wang, W., Liang, Y., and Li, Y.: Full-coverage mapping high-resolution atmospheric CO<sub>2</sub> concentrations in China from 2015 to 2020: Spatiotemporal variations and coupled trends with particulate pollution, *Journal of Cleaner Production*, 428,



- 695 139290, 2023a.
- He, S., Yuan, Y., Wang, Z., Luo, L., Zhang, Z., Dong, H., and Zhang, C.: Machine learning model-based estimation of XCO<sub>2</sub> with high spatiotemporal resolution in china, *Atmosphere*, 14, 436, 2023b.
- He, Z., Fan, G., Li, X., Gong, F.-Y., Liang, M., Gao, L., and Zhou, M.: Spatio-temporal modeling of satellite-observed CO<sub>2</sub> columns in China using deep learning, *International Journal of Applied Earth Observation and Geoinformation*, 129, 103859, 2024.
- 700 He, Z., Lei, L., Zhang, Y., Sheng, M., Wu, C., Li, L., Zeng, Z.-C., and Welp, L. R.: Spatio-temporal mapping of multi-satellite observed column atmospheric CO<sub>2</sub> using precision-weighted kriging method, *Remote Sensing*, 12, 576, 2020.
- 705 Hua, Y., Zhao, X., Sun, W., and Sun, Q.: Satellite-Based Reconstruction of Atmospheric CO<sub>2</sub> Concentration over China Using a Hybrid CNN and Spatiotemporal Kriging Model, *Remote Sensing*, 16, 2433, 2024.
- Huang, N., Gu, L., Black, T. A., Wang, L., and Niu, Z.: Remote sensing-based estimation of annual soil respiration at two contrasting forest sites, *Journal of Geophysical Research: Biogeosciences*, 710 120, 2306-2325, 2015.
- Huang, X., Deng, Z., Jiang, F., Zhou, M., Lin, X., Liu, Z., and Peng, M.: Improved consistency of satellite XCO<sub>2</sub> retrievals based on machine learning, *Geophysical Research Letters*, 51, e2023GL107536, 2024a.
- 715 Huang, X., Yang, H., Lv, Q., Fan, H., Cui, L., Qiao, Y., Yao, Y., and Feng, G.: A full-coverage daily XCO<sub>2</sub> dataset in China from 2015 to 2020 based on DSC-DF-LGB, *Earth System Science Data Discussions*, 2024, 1-22, 2024b.
- Huang, Y., Wang, R., Ju, M., Zhu, X., and Xie, Y.: Reconstructing global daily XCO<sub>2</sub> at 1×1 spatial resolution from 2016 to 2019 with multisource satellite observation data, *Journal of Applied Remote Sensing*, 18, 028502-028502, 2024c.
- 720 Jacobson, A., Schuldt, K., Tans, P., Andrews, A., Miller, J., Oda, T., Mund, J., Weir, B., Ott, L., and Aalto, T.: CarbonTracker CT2022, NOAA Global Monitoring Laboratory, 2023.
- Jin, C., Xue, Y., Jiang, X., Zhao, L., Yuan, T., Sun, Y., Wu, S., and Wang, X.: A long-term global XCO<sub>2</sub> dataset: Ensemble of satellite products, *Atmospheric Research*, 279, 106385, 2022.
- 725 Kemp, L., Xu, C., Depledge, J., Ebi, K. L., Gibbins, G., Kohler, T. A., Rockström, J., Scheffer, M., Schellnhuber, H. J., and Steffen, W.: Climate endgame: Exploring catastrophic climate change scenarios, *Proceedings of the National Academy of Sciences*, 119, e2108146119, 2022.
- Kim, J.-S., Kug, J.-S., Yoon, J.-H., and Jeong, S.-J.: Increased atmospheric CO<sub>2</sub> growth rate during El Niño driven by reduced terrestrial productivity in the CMIP5 ESMs, *Journal of Climate*, 29, 8783-8805, 2016.
- 730 Kuze, A., Suto, H., Nakajima, M., and Hamazaki, T.: Thermal and near infrared sensor for carbon observation Fourier-transform spectrometer on the Greenhouse Gases Observing Satellite for greenhouse gases monitoring, *Applied optics*, 48, 6716-6733, 2009.
- Lee, H., Calvin, K., Dasgupta, D., Krinner, G., Mukherji, A., Thorne, P., Trisos, C., Romero, J., Aldunce, P., and Barret, K.: IPCC, 2023: Climate change 2023: Synthesis report, summary for policymakers. Contribution of working groups I, II and III to the sixth assessment report of the intergovernmental panel on climate change [core writing team, h. Lee and j. Romero (eds.)]. IPCC, Geneva, Switzerland, 2023.
- 735 Lee, J., Jeong, S., Kim, Y. J., Roh, S., Kim, J., and Jin, H.: Synergy of multiple-satellite measurements



- to fill the gap of global XCO<sub>2</sub>, *Journal of Geophysical Research: Atmospheres*, 130, e2024JD042809, 2025.
- 740 Li, J., Jia, K., Wei, X., Xia, M., Chen, Z., Yao, Y., Zhang, X., Jiang, H., Yuan, B., and Tao, G.: High-spatiotemporal resolution mapping of spatiotemporally continuous atmospheric CO<sub>2</sub> concentrations over the global continent, *International Journal of Applied Earth Observation and Geoinformation*, 108, 102743, 2022.
- 745 Li, K., Bai, K., Jiao, P., Chen, H., He, H., Shao, L., Sun, Y., Zheng, Z., Li, R., and Chang, N.-B.: Developing unbiased estimation of atmospheric methane via machine learning and multiobjective programming based on TROPOMI and GOSAT data, *Remote Sensing of Environment*, 304, 114039, 2024a.
- Li, R., Zhou, X., Cheng, T., Tao, Z., Wang, N., Zhang, H., and Lv, T.: Improving Satellite XCO<sub>2</sub> Measurements Accuracy: A Bayesian Bias Correction Approach Considering Spatiotemporal Bias Characteristics, *IEEE Transactions on Geoscience and Remote Sensing*, 2024b.
- 750 Li, Y., Yan, J., Zhong, L., Bao, D., Sun, L., and Li, G.: Full-Coverage Mapping of Daily High-Resolution XCO<sub>2</sub> across China from 2015 to 2020 by Deep Learning-Based Spatio-Temporal Fusion, *IEEE Transactions on Geoscience and Remote Sensing*, 2025.
- 755 Liang, A., Pang, R., Chen, C., and Xiang, C.: XCO<sub>2</sub> Fusion algorithm based on multi-source greenhouse gas satellites and carbontracker, *Atmosphere*, 14, 1335, 2023.
- Liu, W., Li, R., Cao, J., Huang, C., Zhang, F., and Zhang, M.: Mapping high-resolution XCO<sub>2</sub> concentrations in China from 2015 to 2020 based on spatiotemporal ensemble learning model, *Ecological Informatics*, 83, 102806, 2024.
- 760 Liu, Z., Deng, Z., Zhu, B., Ciais, P., Davis, S. J., Tan, J., Andrew, R. M., Boucher, O., Arous, S. B., and Canadell, J. G.: Global patterns of daily CO<sub>2</sub> emissions reductions in the first year of COVID-19, *Nature Geoscience*, 15, 615-620, 2022.
- Lundberg, S. M. and Lee, S.-I.: A unified approach to interpreting model predictions, *Advances in neural information processing systems*, 30, 2017.
- 765 Ma, X., Zhang, H., Han, G., Mao, F., Xu, H., Shi, T., Hu, H., Sun, T., and Gong, W.: A regional spatiotemporal downscaling method for CO<sub>2</sub> columns, *IEEE Transactions on Geoscience and Remote Sensing*, 59, 8084-8093, 2021.
- Petzold, A., Thouret, V., Gerbig, C., Zahn, A., Brenninkmeijer, C. A., Gallagher, M., Hermann, M., Pontaud, M., Ziereis, H., and Boulanger, D.: Global-scale atmosphere monitoring by in-service aircraft—current achievements and future prospects of the European Research Infrastructure IAGOS, *Tellus B: Chemical and Physical Meteorology*, 67, 28452, 2015.
- 770 Qu, Y., and Wei, J., *GlobalHighXCO<sub>2</sub>: Global Daily Seamless 10 km XCO<sub>2</sub> Dataset Over Land (2003–Present)*. <https://doi.org/10.5281/zenodo.182209612026>
- 775 Qu, Y., Wei, J., Xing, H., Shi, X., Ao, Z., and Meng, X.: Global estimates of daily gapless atmospheric XCH<sub>4</sub> concentrations from satellite and reanalysis data during 2003–2020, *IEEE Transactions on Geoscience and Remote Sensing*, 2025.
- Reuter, M., Buchwitz, M., Schneising, O., Krautwurst, S., O'Dell, C. W., Richter, A., Bovensmann, H., and Burrows, J. P.: Towards monitoring localized CO<sub>2</sub> emissions from space: co-located regional CO<sub>2</sub> and NO<sub>2</sub> enhancements observed by the OCO-2 and S5P satellites, *Atmospheric Chemistry and Physics*, 19, 9371-9383, 2019.
- 780 Reuter, M., Bovensmann, H., Buchwitz, M., Burrows, J., Connor, B., Deutscher, N. M., Griffith, D., Heymann, J., Keppel-Aleks, G., and Messerschmidt, J.: Retrieval of atmospheric CO<sub>2</sub> with



- enhanced accuracy and precision from SCIAMACHY: Validation with FTS measurements and comparison with model results, *Journal of Geophysical Research: Atmospheres*, 116, 2011.
- 785 Rodrigues, A., Albuquerque Sardinha, R., and Pita, G.: Fundamentals of global carbon budgets and climate change, in: *Fundamental Principles of Environmental Physics*, Springer, 303-351, 2025.
- Romanov, V.: *Greenhouse Gases and Clay Minerals: Enlightening Down-to-Earth Road Map to Basic Science of Clay-Greenhouse Gas Interfaces*, Springer2017.
- 790 Sheng, M., Lei, L., Zeng, Z.-C., Rao, W., and Zhang, S.: Detecting the responses of CO<sub>2</sub> column abundances to anthropogenic emissions from satellite observations of GOSAT and OCO-2, *Remote Sensing*, 13, 3524, 2021.
- Sheng, M., Lei, L., Zeng, Z.-C., Rao, W., Song, H., and Wu, C.: Global land 1° mapping dataset of XCO<sub>2</sub> from satellite observations of GOSAT and OCO-2 from 2009 to 2020, *Big Earth Data*, 7, 170-190, 2023.
- 795 Siabi, Z., Falahatkar, S., and Alavi, S. J.: Spatial distribution of XCO<sub>2</sub> using OCO-2 data in growing seasons, *Journal of environmental management*, 244, 110-118, 2019.
- Tian, W., Zhang, L., Yu, T., Wu, Y., Zhang, W., Wang, Z., and Zhu, H.: Using multi-source data and time series features to construct a global terrestrial CO<sub>2</sub> coverage by deep learning, *IEEE Transactions on Geoscience and Remote Sensing*, 2024.
- 800 Vaswani, A., Shazeer, N., Parmar, N., Uszkoreit, J., Jones, L., Gomez, A. N., Kaiser, Ł., and Polosukhin, I.: Attention is all you need, *Advances in neural information processing systems*, 30, 2017.
- Wang, J., Liu, Z., Zeng, N., Jiang, F., Wang, H., and Ju, W.: Spaceborne detection of XCO<sub>2</sub> enhancement induced by Australian mega-bushfires, *Environmental Research Letters*, 15, 124069, 2020.
- 805 Wang, X., Piao, S., Ciais, P., Friedlingstein, P., Myneni, R. B., Cox, P., Heimann, M., Miller, J., Peng, S., and Wang, T.: A two-fold increase of carbon cycle sensitivity to tropical temperature variations, *Nature*, 506, 212-215, 2014.
- Wang, Y., Yuan, Q., Li, T., Yang, Y., Zhou, S., and Zhang, L.: Seamless mapping of long-term (2010–2020) daily global XCO<sub>2</sub> and XCH<sub>4</sub> from the Greenhouse Gases Observing Satellite (GOSAT), Orbiting Carbon Observatory 2 (OCO-2), and CAMS global greenhouse gas reanalysis (CAMSEGG4) with a spatiotemporally self-supervised fusion method, *Earth System Science Data*, 15, 3597-3622, 2023.
- 810 Wang, Z., Zhang, C., Shi, K., Shanguan, Y., Hu, B., Chen, X., Wei, D., Chen, S., Atkinson, P. M., and Zhang, Q.: A full-coverage satellite-based global atmospheric CO<sub>2</sub> dataset at 0.05° resolution from 2015 to 2021 for exploring global carbon dynamics, *Earth Syst. Sci. Data*, 17, 5355–5375, <https://doi.org/10.5194/essd-17-5355-2025>, 2025.
- Wei, J., Wang, Z., Li, Z., Li, Z., Pang, S., Xi, X., Cribb, M., and Sun, L.: Global aerosol retrieval over land from Landsat imagery integrating Transformer and Google Earth Engine, *Remote Sensing of Environment*, 315, 114404, 2024.
- 820 Wei, J., Li, Z., Chen, X., Li, C., Sun, Y., Wang, J., Lyapustin, A., Brousseau, G. P., Jiang, M., and Sun, L.: Separating daily 1 km PM<sub>2.5</sub> inorganic chemical composition in China since 2000 via deep learning integrating ground, satellite, and model data, *Environmental science & technology*, 57, 18282-18295, 2023.
- 825 Wolter, K. and Timlin, M. S.: El Niño/Southern Oscillation behaviour since 1871 as diagnosed in an extended multivariate ENSO index (MEI. ext), *International Journal of Climatology*, 31, 1074-



- 1087, 2011.
- 830 Wu, C., Yang, S., Jiao, D., Chen, Y., Yang, J., and Huang, B.: Estimation of daily XCO<sub>2</sub> at 1 km resolution in China using a spatiotemporal ResNet model, *Science of The Total Environment*, 954, 176171, 2024.
- Wunch, D., Wennberg, P. O., Osterman, G., Fisher, B., Naylor, B., Roehl, C. M., O'Dell, C., Mandrake, L., Viatte, C., and Kiel, M.: Comparisons of the orbiting carbon observatory-2 (OCO-2) XCO<sub>2</sub> measurements with TCCON, *Atmospheric Measurement Techniques*, 10, 2209-2238, 2017.
- 835 Yang, D., Liu, Y., Cai, Z., Chen, X., Yao, L., and Lu, D.: First global carbon dioxide maps produced from TanSat measurements, 2018.
- Yeom, J.-M., Jeong, S., Ha, J.-S., Lee, K.-H., Lee, C.-S., and Park, S.: Estimation of the hourly aerosol optical depth from GOCI geostationary satellite data: deep neural network, machine learning, and physical models, *IEEE Transactions on Geoscience and Remote Sensing*, 60, 1-12, 2021.
- 840 Zhang, B., Zhang, H., Zhao, G., and Lian, J.: Constructing a PM<sub>2.5</sub> concentration prediction model by combining auto-encoder with Bi-LSTM neural networks, *Environmental Modelling & Software*, 124, 104600, 2020.
- Zhang, L., Li, T., Wu, J., and Yang, H.: Global estimates of gap-free and fine-scale CO<sub>2</sub> concentrations during 2014–2020 from satellite and reanalysis data, *Environment International*, 178, 108057, 2023.
- 845 Zhang, M. and Liu, G.: Mapping contiguous XCO<sub>2</sub> by machine learning and analyzing the spatio-temporal variation in China from 2003 to 2019, *Science of The Total Environment*, 858, 159588, 2023.